Research Article Vol. 32, No. 25 / 2 Dec 2024 / Optics Express 45075
Optics EXPRESS

Chiral optical properties of metasurfaces comprised of chiral media: effects of geometric and material chirality

MAYA RAMAMURTHY, BRYAN M. COTE, AND VIVIAN E. FERRY*

Department of Chemical Engineering and Materials Science, University of Minnesota, 421 Washington Ave. SE, Minneapolis, MN 55455, USA
*veferry@umn.edu

Abstract: We deconvolute the distinct and sometimes competing effects of geometric and material chirality in metastructures created from materials that are intrinsically chiral. We find that overlapping Mie-like resonances in nanodisk arrays leads to 6-fold CD enhancement compared to a uniform film. Furthermore, making the medium chiral does not necessarily increase CD; enhancement depends on the magnitude of the Pasteur parameter and its real and imaginary components. Finally, to demonstrate how geometric and material chirality can be combined, we design a geometrically chiral meta-atom out of chiral media and observe over 9-fold enhancement in both CD and g-factor compared to a metasurface comprised of achiral material.

1. Introduction

Chiral metastructures are attracting increasing attention for a range of different applications, including circularly polarized light detectors and sources [1–5], enantiospecific catalysis, separation and detection [6–10], and spintronics and quantum computing [11,12]. For example, strategic design of metasurfaces can lead to strongly enhanced circular dichroism (CD) compared to chiral molecules, or create superchiral light for improved detection of chiral analytes [13,14]. A recurring challenge, however, is to identify the design rules that govern chiral response from these metasurfaces, as the relationship between the optical properties and the structure is complex.

In much of the work done to-date, the material comprising the metasurface is achiral. Previous work using metastructures to detect chiral analytes has pointed to the importance of overlapping the electric dipole and magnetic dipole resonances of a disk to enhance the local optical chirality [15–19]. When the electric and magnetic resonances spectrally overlap with equal magnitude and a $\pi/2$ phase difference, backscattering is suppressed and the Kerker condition for circularly polarized light is satisfied [20]. In several studies, satisfying the Kerker conditions has led to enhanced optical chirality [13,21]. However, these applications mainly consider the detection of chiral media nearby the metasurface, rather than within the nanostructure itself. Here, we expand our study beyond molecular sensing near the metasurface to applications where the local optical chirality inside the nanostructure is important.

An interesting question is whether the chiral optical properties of the metasurface are enhanced if the material itself is chiral (or, alternatively, if the properties of a chiral material are enhanced by nanostructuring). There are numerous emerging examples of candidate chiral materials, including chiral molecules and semiconductor nanocrystals [22–31]. These chiral nanomaterials can be further organized into superstructures of various types, which may or may not have geometric chirality. However, both ligand-induced chiral semiconductor nanocrystals and molecules are often limited by low levels of selectivity for circularly polarized light, with g-factors often on the order of 10^{-5}–10^{-3}, while typical CD signals of metasurfaces are on the order of 10^{-2} deg [22].

#540182 https://doi.org/10.1364/OE.540182
Journal © 2024 Received 28 Aug 2024; revised 1 Nov 2024; accepted 5 Nov 2024; published 27 Nov 2024

Optics EXPRESS

Optical design could therefore include either or both geometric and material chirality, and the relationship between the two warrants deeper research.

In this paper, we focus primarily on modeling materials with properties inspired by chiral semiconductor nanocrystals and the lithographic patterning and self-assembly of chiral nanostructures demonstrated in previous studies [32,33]. In cases where the chiral nanostructures are themselves comprised of either strongly absorbing or light-emitting chiral nanocrystals, then the CD or circularly polarized luminescence from the array could be influenced by the optical chirality inside the nanostructures. We investigate the role of the nanostructure size, shape, and accompanying resonances, and the characteristics of the materials themselves, including the role of Pasteur parameter, on CD, g-factor, optical chirality, and the difference in transmission (ΔT) under polarized illumination, with both achiral and chiral geometries. We find that designing a disk array made of chiral media with spectrally overlapping electric and magnetic dipolar Mie-like resonances enhances the CD compared to a uniform film. We also find that simply increasing the Pasteur parameter does not necessarily further increase the optical chirality enhancement. Through strategic choices of the Pasteur parameter, we demonstrate optical chiralities 50 times larger than free space circularly polarized light and ΔT enhancements over 750-fold compared to unstructured films. Additionally, matching the Mie-like resonances of the disk array to the chiral material's Lorentzian transitions creates a combined CD enhancement that is greater than the sum of the individual effects of disk geometry and excitonic transitions. Finally, we design a metasurface array that combines the effects of a chiral meta-atom geometry with a chiral medium, thereby enhancing the CD and g-factor by utilizing geometrical and material chirality at the same time. This work highlights both the potential and complexity of creating chiral nanomaterials, where the roles of both material and geometric chirality need to be understood.

2. Method

The circular dichroism of optically active thin-films and disk arrays like those shown in Fig. 1 were modeled using COMSOL Multiphysics. Multiple relations for chiral media have been developed [34,35] with the most common including the introduction of the Pasteur parameter, κ. To study optically active materials using finite element methods, Maxwell's equations must be modified to allow for magnetoelectric coupling, as shown in Eq. (1) and Eq. (2) [36,37].

$$\boldsymbol{D} = \varepsilon \boldsymbol{E} - i\kappa\sqrt{\mu_0\varepsilon_0}\boldsymbol{H} \tag{1}$$

$$\boldsymbol{B} = \mu \boldsymbol{H} + i\kappa\sqrt{\mu_0\varepsilon_0}\boldsymbol{E} \tag{2}$$

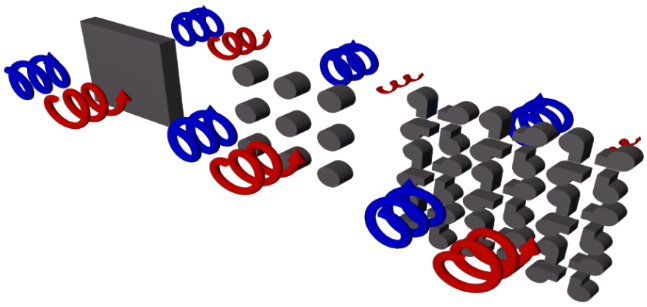

Fig. 1. Schematic depiction of circular dichroism measurement through a uniform film of chiral material, a patterned disk array, and a patterned array made of geometrically chiral meta-atoms.

The introduction of the Pasteur parameter introduces circular polarization dependence to the refractive index of the chiral medium, such that $n_{\pm} = n \pm \kappa$. The Pasteur parameter can be real,

Optics EXPRESS

imaginary, or complex. The real part of κ represents the optical rotary dispersion (ORD) of the chiral medium, which is rotation of linearly polarized light upon passing through the chiral sample. The imaginary part of κ controls the circular dichroism of the chiral medium.

Circularly polarized light was included in our simulations by defining ±90° phase shifts in the x and y components of the electric field amplitudes at the injection ports. Periodic boundary conditions were placed on simulation bounds perpendicular to the circularly polarized source and perfectly matched layer boundary conditions were included at the top and bottom simulation bounds. Lastly, the absorption within the metasurfaces and planar thin films was calculated by considering both transmission and reflection, where $A = -\log_{10}(T + R)$. The CD is defined as the difference in absorption of left versus right circularly polarized (LCP/RCP) light and is given by $CD = A_{LCP} - A_{RCP}$. CD is often reported in units of degrees, where $CD\ [deg] = 32.98 \times \Delta A$. The g-factor normalizes the CD by a chiral analyte's total absorption and is defined as $g = 2 \times (A_{LCP} - A_{RCP})/(A_{LCP} + A_{RCP})$.

3. Results and discussion

3.1. Disk arrays comprised of chiral material

We begin by considering the effect of nanostructuring, and particularly the design of resonant meta-atoms, on the chiroptical properties of metamaterials comprised of chiral media. We first consider the case of a simple disk array, as illustrated in Fig. 1, and identify the disk geometries that lead to overlapping the electric and magnetic dipolar Mie-like resonances. To design the disks, we assumed a constant refractive index of $n = 2$ - $0.1i$, $\kappa = $ -$0.0005i$, a height of $h = 200$ nm, and spacing in a square array with a $p = 650$ nm pitch. The disk's refractive index was chosen to approximate that of a semiconductor nanocrystal solid [33]. We varied the disk diameter, since the resonant frequencies of the electric and magnetic dipolar resonances in a disk array can be independently tuned by varying the disk's aspect ratio [13,38].

Figure 2(a) shows the transmittance of constant refractive index disk arrays under linearly polarized (LP) illumination. At certain wavelengths, large minima in transmission are present, due to the excitation of Mie-like resonances. The resonant characters of the transmission minima were evaluated by measuring the electromagnetic intensity enhancement in the center of the disks. The wavelength of maximum electric (magnetic) field intensity enhancement at the disk's center corresponds to the resonant wavelength of an electric (magnetic) dipolar resonance [13]. Both the electric and magnetic dipolar (ED and MD) resonances redshift with increasing disk diameter but at different rates, allowing for spectral overlap of the resonances to be tuned. Spectral overlap is observed at two disk diameters: $d = 325$ nm and $d = 468$ nm. To evaluate whether the overlapping Mie-like resonances at these disk geometries constitute Kerker conditions, which occur when the reflection is identically zero, the reflection spectrum is shown in Fig. 2(b). The disk array made up of $d = 325$ nm disks reflects almost 20% of incident light at the resonant wavelength ($\lambda = 695$ nm). By contrast, the disk array made up of $d = 468$ nm disks reflects less than 5% of incident light at its corresponding resonant wavelength ($\lambda = 760$ nm). As a result, we will call the $d = 468$ nm disk array at $\lambda = 760$ nm a Kerker-like condition. Note that for this disk geometry, the reflection also approaches zero near $\lambda = 690$ nm, but the ED and MD resonances do not overlap here. To achieve maximal optical chirality enhancement, the electric and magnetic fields must be spatially overlapped [13,21]. Figure 2(c) shows the spatial distribution of the electric and magnetic resonances in the center of a $d = 468$ nm disk at $\lambda = 760$ nm. Both the electric and magnetic fields are maximized in the center of the disk. For comparison, the spatial field distribution for the $d = 325$ nm disk array at $\lambda = 695$ nm is shown in Fig. 2(d). The electric and magnetic fields are spatially overlapped inside the disk and the electric field inside the disk is larger than it is for the $d = 468$ nm disk. However, the electric field is maximized outside the disk, not in the center.

Optics EXPRESS

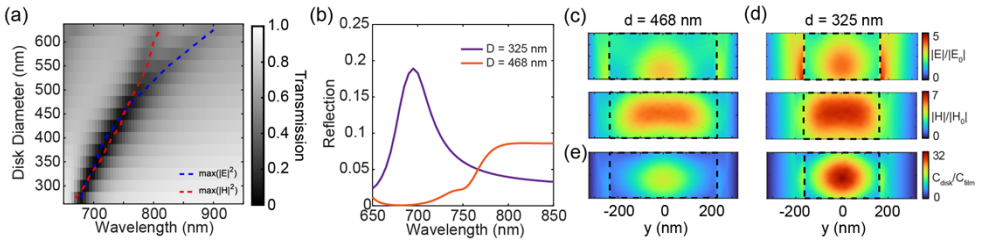

Fig. 2. (a) Transmission of LP light through chiral disk arrays of various diameters and (b) reflection from disk arrays with diameters that support overlapping Mie-like resonances. Electric and magnetic field intensity enhancements in the center of a (c) $d = 468$ nm disk at $\lambda = 760$ nm and (d) $d = 325$ nm disk at $\lambda = 695$ nm. (e) Optical chirality enhancement relative to a uniform film for (left) a $d = 468$ nm disk at $\lambda = 760$ nm and (right) a $d = 325$ nm disk at $\lambda = 695$ nm.

We now compare the calculations of chiroptical response between the disk and an unstructured film of chiral material. The optical chirality, C, is given by $C = -\omega\varepsilon_0 \times \mathrm{Im}(\boldsymbol{E}^* \cdot \boldsymbol{H})/2$ and optical chirality enhancement, $\hat{C}$, is given by, $\hat{C} = C/C_{CPL} = \mathrm{Im}(\mathbf{E}^* \cdot \boldsymbol{H})/\mathrm{Im}(\mathbf{E}^* \cdot \boldsymbol{H})_{CPL}$. Optical chiralities greater than free space circularly polarized light ($\hat{C}$>1) are often referred to as superchiral. Overlapping electric and magnetic modes lead to overlapping $\boldsymbol{E}$ and $\boldsymbol{H}$ fields, generating superchiral near-fields of a uniform sign [13,21]. Fig. 2(e) shows the optical chirality enhancement for a $d = 468$ nm disk at $\lambda = 760$ nm, relative to a 200 nm thick film with the same refractive index and Pasteur parameter. Figure 2(f) compares this to the optical chirality enhancement for a $d = 325$ nm disk at $\lambda = 695$ nm. The optical chirality enhancement both inside the disk and around it is larger for the $d = 325$ nm disk. This is consistent with the larger electric and magnetic field intensity compared to the $d = 468$ nm disk.

Figure 3 shows the optical chirality enhancement, CD enhancement, and g-factor enhancement for chiral disks compared to a uniform film. Figure 3(a) shows the spatially averaged optical chirality enhancement ($(C_l + C_r)/2$) within the disks. This calculation is relevant to systems where light-emitting nanocrystals comprise the meta-atoms, such as circularly polarized light sources. At each diameter, the optical chirality is high at the resonant wavelength, at similar wavelengths as shown in Fig. 2. At $d = 468$ nm and $\lambda = 760$ nm, excitation of both electric and magnetic dipolar resonances at the Kerker-like condition results in a volume-averaged optical chirality enhancement of 7-fold compared to the film. The maximum in optical chirality enhancement occurs at $d = 325$ nm and $\lambda = 695$ nm. $C_{Disk}\,/C_{Film}$ is larger here because both the ED and MD are larger than at $d = 468$ nm, $\lambda = 760$ nm ($|\mathrm{E}|/|\mathrm{E}_0|$: 3.7 vs 2.8, $|\mathrm{H}|/|\mathrm{H}_0|$: 6.1 vs 5.4). Since $d = 325$ nm does not constitute a Kerker condition, we hypothesize that the reflected fields are contributing in-part to the enhanced optical chirality. This is consistent with the $\boldsymbol{E}$ and $\boldsymbol{H}$ fields being less spatially confined inside the $d = 325$ nm disk compared to inside the $d = 468$ nm disk (vide supra, Fig. 2). If the disks are comprised of luminescent semiconductor nanocrystals, the enhanced optical chirality within the disks could lead to enhanced circularly polarized light emission from the array. This is a topic of future research.

Figure 3(b) shows the spectrally resolved CD enhancement ($[CD]_{disk}/[CD]_{film}$) for the same disk diameters and wavelengths. The CD enhancement is maximized for the $d = 468$ nm disk array, or in other words, at the Kerker-like condition. Here, there is a maximum CD enhancement of 5.7-fold at $\lambda = 760$ nm, despite containing 28% less chiral material than the planar thin film. The sign of the CD enhancement is negative because the sign of the film CD is opposite that of the disk CD near the Kerker-like condition. Notably, the CD enhancement at $d = 325$ nm and $\lambda = 695$ nm is quite small (1.7-fold). This is because we have considered reflection in our definition of CD ($A = -\log_{10}(T + R)$) and the $d = 325$ nm disk array reflects significantly more

Optics EXPRESS

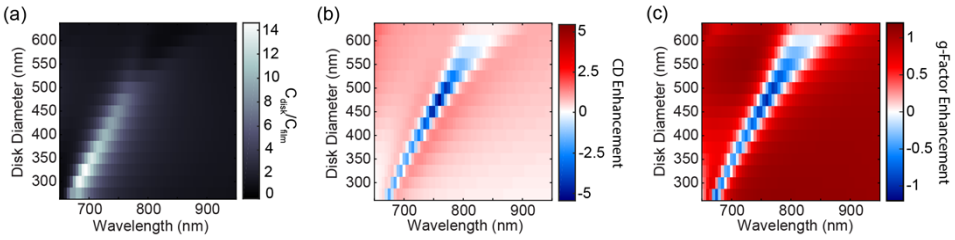

Fig. 3. Spectrally resolved (a) average optical chirality enhancement, (b) CD enhancement, and (c) g-factor enhancement for various chiral disk array diameters relative to an unstructured film of chiral media.

light than the $d = 468$ nm array (vide supra, Fig. 2(b)). This analysis shows that the optimal geometries for optical chirality enhancement and CD enhancement are not always the same when reflection is taken into consideration.

In many applications, increasing the selectivity of circularly polarized absorption is even more desirable than increasing the magnitude of circular dichroism signal. However, Fig. 3(c) shows that, at the spectrally overlapping ED and MD resonances, the magnitude of the g-factor is comparable to that of the film. This is because the nanostructures enhance overall absorption by over 7-fold at the Kerker-like condition compared to the film, while the corresponding CD enhancement is 5.7-fold. As a result, the circularly polarized absorption selectivity is decreased.

3.2. Modifying the Pasteur parameter

3.2.1. Purely real-valued Pasteur parameter

We now consider how different chiral media influence these design guidelines. The Pasteur parameter used in the previous analysis ($\kappa = -0.0005i$) was chosen as a starting point for investigation. However, many chiral molecules have negligible absorption in the visible and near-IR region of the spectrum and have purely real Pasteur parameters [39]. Typical values of the Pasteur parameter for chiral liquids with low dispersion like limonene and carvone are on the order of $\kappa = 0.01$ in the visible range [39–41]. To investigate the case of a purely real Pasteur parameter, we consider a Mie-like disk array with $n = 2$ and $d = 457$ nm, with the same height and pitch as before ($h = 200$ nm, $p = 650$ nm). In Fig. 4(a), we vary the magnitude of the real part of the Pasteur parameter. For these nonabsorbing arrays, rather than calculating CD, we calculate the difference in transmitted LCP versus RCP light ($\Delta T = T_{LCP} - T_{RCP}$). The ΔT enhancement for the disk array relative to a uniform film with the same properties ($[\Delta T]_{disk}/[\Delta T]_{film}$) increases in magnitude with increasing κ, along with increasing spectral separation of the positive and negative ΔT features. When $\kappa = 0.01$, ΔT enhancement of over 750-fold is achieved and when $\kappa = 0.1$, ΔT enhancement of over 3000-fold is possible.

The dependence of ΔT enhancement on κ involves several different factors, not just increasing Pasteur parameter. Figure 4(b)-(c) show that the ΔT enhancement increases with κ in this geometry because the disk array supports spectral maxima in ΔT that increase much faster than the spectrally featureless ΔT generated by the film. Increasing the Pasteur parameter also increases the spectral separation between the positive and negative ΔT features, where $\Delta\lambda = 8$ nm for $\kappa = 0.01$ and $\Delta\lambda = 30$ nm for $\kappa = 0.1$ (Fig. 4(b)). The increasing spectral separation with κ arises because the resonant frequencies under right versus left CPL shift and become more distinct as κ increases. Figure 4(d) demonstrates this by plotting the optical chirality of the disk array as the Pasteur parameter varies. When the Pasteur parameter is small ($\kappa = 0.001$-0.01), the optical chirality is maximized at the resonant wavelength ($\lambda = 750$ nm). For these two cases, the optical chirality is over 50 times larger than free space circularly polarized light (CPL). As the Pasteur parameter increases in magnitude, the maximum in the optical chirality under left CPL

Optics EXPRESS

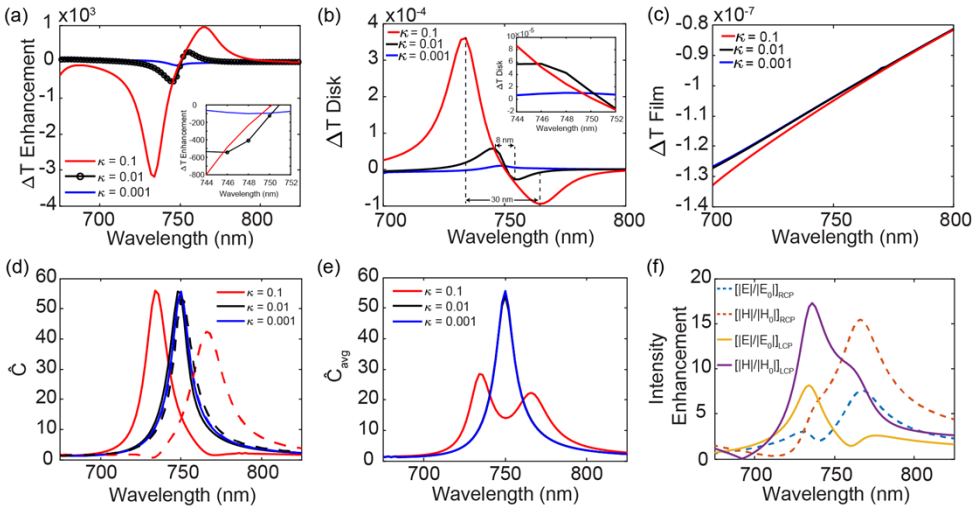

Fig. 4. Effect of different values of a purely real Pasteur parameter for a resonant disk array with $p = 650$ nm, $h = 200$ nm, $d = 457$ nm, and $n = 2$. (a) ΔT enhancement compared to a uniform film, (b) ΔT of the disk array, and (c) ΔT of the uniform film. Inset in (a) and (b) shows enlarged region around $\lambda = 750$ nm. (d) Volume-averaged optical chirality within the disks, where dashed lines represent RCP light and solid lines represent LCP light. (e) Average optical chirality under LP light. (f) Field intensity enhancement within a disk when $\kappa = 0.1$, where dashed lines represent RCP light and solid lines represent LCP light.

becomes spectrally separated from the maximum under right CPL. This phenomenon is best observed with high κ, since this case results in the largest difference in refractive index between the two incident polarizations. When $\kappa = 0.1$, the maxima in optical chirality are shifted by ∓ 16 nm under right versus left CPL. One consequence of this is diminished optical chirality under RCP incident light compared to the system with smaller values of κ. The spectral separation and diminished optical chirality under RCP light results in a significantly smaller average optical chirality when $\kappa = 0.1$ ($\hat{C}_{max} = 28$) compared to when $\kappa = 0.001$-0.01 ($\hat{C}_{max} = 56$), as shown in Fig. 4(e). This also leads to the asymmetric ΔT enhancement spectra seen in Fig. 4(a) for $\kappa = 0.1$, where the wavelength and relative magnitude of the peak in optical chirality for LCP (RCP) light matches that of the dip (peak) in ΔT enhancement.

Evidence that spectral shifting of the maximum in optical chirality under different incident polarizations is a consequence of shifting Mie-like resonances is provided in Fig. 4(f), which shows the electric and magnetic field intensity enhancement at the center of the $\kappa = 0.1$ disk. For an array made of achiral material, the electric and magnetic field intensity enhancement spectra are the same under left and right circularly polarized illumination [35]. When $\kappa = 0.1$ the maximum in magnetic field intensity enhancement under LCP light is larger than under RCP light, which explains the larger optical chirality and magnitude of ΔT enhancement at the corresponding wavelength ($\lambda = 734$ nm). The magnetic field intensity enhancement spectra in Fig. 4(f) also show a secondary peak at $\lambda = 760$ nm for LCP light and $\lambda = 740$ nm for RCP light. These peaks arise due to the magnetoelectric coupling that becomes significant at high κ. When κ is real and positive, magnetoelectric coupling results in a minimum in the electric field and an increase in the magnetic field (see Eq. (1) and Eq. (2)). We observe that electric quadrupoles exist where these minima in electric field occur (at $\lambda = 760$ nm and $\lambda = 740$ nm), whereas electric dipoles exist at the maxima of the electric field intensity spectra ($\lambda = 734$ nm and $\lambda = 766$ nm). The additional peaks in the magnetic field intensity spectra are not observed for disk arrays with smaller κ ($\kappa \leq 0.01$).

Optics EXPRESS

This analysis shows that, for a given metasurface geometry with a real-valued Pasteur parameter, changing the magnitude of the Pasteur parameter spectrally shifts the absolute ΔT and ΔT enhancement, in addition to changing the magnitude. One consequence of this spectral shifting is that at certain wavelengths (e.g. $\lambda = 748$ nm), simply increasing the value of κ (for example from $\kappa = 0.01$ to 0.1) will not increase the ΔT or ΔT enhancement (see Fig. 4(a)-(b), inset); the geometry of the metasurface needs to be reoptimized. This spectral shifting should be accounted for when designing metastructures comprised of media with large real Pasteur parameters. Additionally, increasing κ (i.e. from $\kappa = 0.01$ to 0.1) diminishes both polarization-specific optical chirality and the average optical chirality. Currently the polarization efficiency of ΔT for the disk array is low ($\frac{2\times(T_{LCP}-T_{RCP})}{T_{LCP}+T_{RCP}} \sim 4.4 \times 10^{-4}$ for $\kappa = 0.1$), and increasing this efficiency, perhaps by changing the metasurface geometry, could be a topic of future research. Increasing κ will introduce stronger magnetoelectric coupling which alters the shape of the electric and magnetic field intensity spectra in a nonobvious way that is not observed at smaller κ.

3.2.2. Purely imaginary-valued Pasteur parameter

Although $Re(\kappa) \gg Im(\kappa)$ for most realistic chiral systems, the Pasteur parameter can be purely imaginary at the center wavelength of a Lorentzian medium, where κ is highly dispersive [42]. The impact of the magnitude of the imaginary part of the Pasteur parameter on the CD enhancement of a disk array with $d = 468$ nm and $n = 2$–$0.1i$ is investigated in Fig. 5. Figure 5(a) shows that the magnitude of the CD enhancement stays consistent (6-fold enhancement) as the magnitude of the purely imaginary Pasteur parameter increases. This is different from the case of a purely real Pasteur parameter and occurs because the CD of the film increases proportionally to the CD of the disk when $|\kappa|$ is increased (Fig. 5(b)-(c)). Furthermore, when κ is purely imaginary, the system only supports one CD spectral feature, and this occurs at the resonant wavelength.

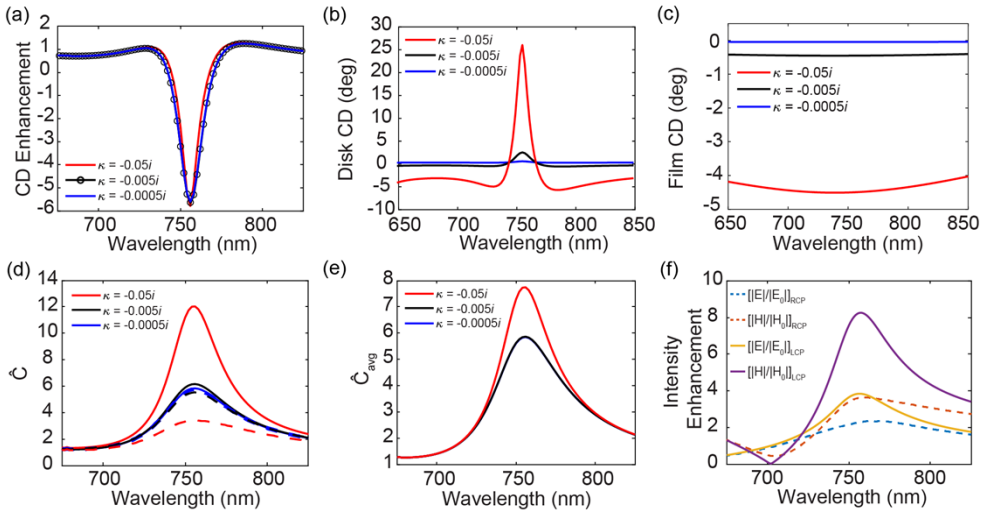

Fig. 5. Effect of different values of a purely imaginary Pasteur parameter for a resonant disk array with $p = 650$ nm, $h = 200$ nm, $d = 468$ nm, and $n = 2$ - $0.1i$. (a) CD enhancement compared to a uniform film. CD of (b) the disk array and (c) the uniform film only. (d) Volume-averaged optical chirality within the disks, where dashed lines represent RCP light and solid lines represent LCP light. (e) Average optical chirality under LP light. (f) Field intensity enhancement within a disk when $\kappa = -0.05i$, where dashed lines represent RCP light and solid lines represent LCP light.

Optics EXPRESS

The CD enhancement does not spectrally shift like it does for the case of purely real κ because increasing the magnitude of the purely imaginary κ changes only the magnitude of the optical chirality under right versus left CPL. This is shown in Fig. 5(d) and is especially apparent in the medium where $\kappa = -0.05i$, which demonstrates over 3 times more optical chirality when illuminated with LCP light (solid line) compared to RCP light (dashed line) at the resonant wavelength of 760 nm. This is consistent with Fig. 5(f), which shows that the electric and magnetic field intensity spectra increase in magnitude under LCP light (compared to RCP light), but mostly retain the same spectral shape and position. Since the ED and MD maxima occur at the same wavelength for both RCP and LCP light, the effect of increasing $|\kappa|$ on optical chirality is additive. Therefore, the average optical chirality increases as $|\kappa|$ is increased from $-0.005i$ to $-0.05i$ ($\hat{C}_{max}$ increases from roughly 6 to roughly 8), unlike the analogous result for purely real Pasteur parameter (Fig. 5(e)). This means that both optical chirality and CD at a particular wavelength can be increased by increasing the magnitude of the imaginary part of the Pasteur parameter, without the need to reoptimize the array geometry.

Taken together, the results in Fig. 4 and Fig. 5 show that Mie-like disk arrays with a purely real Pasteur parameter and a physically relevant refractive index ($n = 2$) show large differential transmission of left versus right CPL compared to a uniform film. Further, the spectral shifting with increasing Pasteur parameter adds an additional layer of complexity to increasing the optical chirality and differential transmission of left versus right CPL. By comparison, Mie-like disk arrays with a purely imaginary Pasteur parameter and refractive index $n = 2–0.1i$ have more moderate CD enhancements that don't increase with $|\kappa|$ and optical chirality that does not spectrally shift with $|\kappa|$.

3.2.3. Effect of a complex and dispersive chiral medium

At most wavelengths, the Pasteur parameters of real chiral materials are not purely real or imaginary, but complex and dispersive. We considered the effects of dispersion by modeling a chiral, Lorentzian medium. The dispersion equations for the chiral medium's permittivity and Pasteur parameter are given by $\varepsilon = 4 - 10^{-3} \times \bar{\omega}$ and $\kappa = -10^{-5} \times \bar{\omega}$, respectively, where $\bar{\omega} = \omega_0^2/(\omega^2 - \omega_0^2 - i\gamma\omega)$ and the center frequency, $\omega_0 = 2\pi c/\lambda_0$, was tuned on and off the Kerker-like condition of $\lambda = 760$ nm while the damping constant, $\gamma = \pi c(1/(\lambda_0 - FWHM) - 1/(\lambda_0 + FWHM))$, was set to give the Lorentzian a full width at half maximum of approximately 20 nm [43,44]. Fig. 6(a)-(b) show the spectral dependence of the real and imaginary Pasteur parameter, respectively. Figure 6(c) compares the CD of a $d = 468$ nm disk array to that of a uniform film at several different center frequencies. These frequencies represent the wavelength where the Kerker-like condition occurs for a $d = 468$ nm disk ($\lambda = 760$ nm), and wavelengths ±40 nm of this condition. For both cases away from the Kerker-like condition, the disk arrays show two CD minima, one at the center frequency and the other at the wavelength where the Kerker-like condition occurs ($\lambda = 760$ nm). The local minimum in CD at the center frequency is due to the Lorentzian transition. The local minimum in CD at $\lambda = 760$ nm is due to the Mie-like resonance. This is further supported by the fact that the uniform film only shows a single CD minimum at the center frequency.

Matching the Mie-like resonances to the chiral material's Lorentzian transitions maximizes the CD and results in a nearly 22-fold CD enhancement (3.4-fold g-factor enhancement) compared to the film, as shown in Fig. 6(d). At wavelengths on either side of the center wavelength, the CD of the disk is greater than that of the film, but the difference is negligible. Therefore, spectrally overlapping the Mie-like resonances with the center frequency of the Pasteur parameter enhances the chiroptical response. In this case, the energy states of the Lorentz oscillator and the optical ED and MD modes are coupled together, leading to a hybrid light-matter resonance. This is consistent with previous work studying the CD of a chiral, dielectric nanosphere with a shell of excitonic material given by the Lorentz model [45]. The resulting CD magnitude of the matched

Optics EXPRESS

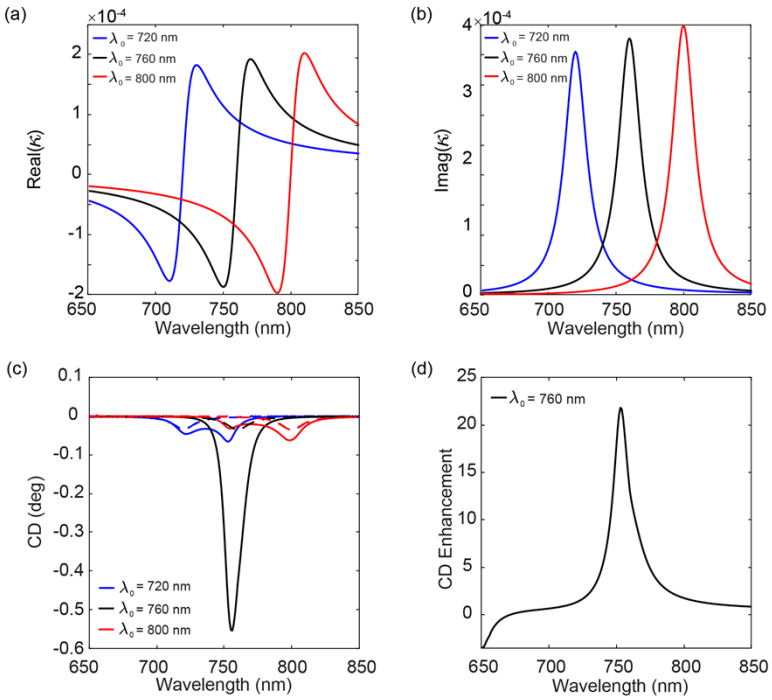

Fig. 6. Spectral dependence of the (a) real Pasteur parameter and (b) imaginary Pasteur parameter for a chiral, Lorentzian disk array. (c) CD of the chiral disk array with $d = 468$ nm and $p = 650$ nm (solid lines) compared to CD of a uniform chiral film (dashed lines). (d) CD enhancement of the chiral disk array compared to the chiral film when $\lambda_0 = 760$ nm.

system is greater than the sum of the individual excitonic or Mie-like resonance effects. This highlights the significant improvement that Mie-like resonances provide to the CD of chiral materials with Lorentzian transitions. By matching the Mie-like resonances to the excitonic transitions, we can tune the chiral response, either by adding new features to the CD spectrum, or by increasing the CD signal.

3.3. *Combining geometric and material chirality*

Several studies have shown that it is possible to have local optical chirality around achiral dielectric nanostructures made of achiral material [13,14,46]. Here, we consider the case where both the shape of the object and the material comprising it are chiral. To investigate this, we modified our disk geometry by adding a short tail. We arranged the structures with C4 rotation symmetry, as shown in Fig. 7(a), to avoid the linear birefringence that arises from the asymmetry between the x and y directions of a single chiral shape [47]. For comparison to an achiral shape, we simulated a C4 symmetric unit cell made of disks with the same refractive index ($n = 2–0.1i$), height ($h = 200$ nm), and pitch ($p = 1300$ nm). To match the CD and g-factor magnitude of the disk array to that of the new chiral meta-atom array, we set the Pasteur parameter of both to $\kappa = -5 \times 10^{-6}i$. The dimensions of the chiral shape (d, s, o, w, 1) were chosen so that the CD and g-factor of the resulting meta-atom would have a local maximum at approximately the same wavelength as the disk array. Figure 7 demonstrates that although chiral patterning is not strictly necessary for achieving a chiral response from dielectric metasurfaces, combining material chirality with geometric chirality is a way to tune both the wavelength and magnitude of the chiral response. Compared to the disk array, structures that have both intrinsic chirality ($\kappa \neq 0$) and a chiral shape

Optics EXPRESS

exhibit a 20% enhancement in CD (Fig. 7(a)) and g-factor (Fig. 7(b)) at the resonant wavelength for the disk array ($\lambda = 760$ nm). Furthermore, these structures (with $\kappa \neq 0$ and a chiral shape) exhibit a 9-fold CD enhancement at $\lambda = 760$ nm compared to metasurfaces where the meta-atom shape is chiral but the comprising material is not ($\kappa = 0$). This demonstrates that for the chiral arrangement in Fig. 7(a), chiral nanopatterning of chiral materials increases both the CD and g-factor at $\lambda = 760$ nm. Figure 7(a) also shows that at some wavelengths smaller than the resonant wavelength (e.g. $\lambda = 740$ nm), the CD and g-factor magnitudes are larger for the disk metasurface compared to the chiral arrangement. At $\lambda = 740$ nm, the CD of the chiral arrangement comprised of chiral material (black line) is nearly zero (0.3 mdeg), while the CD of the disk geometry is over 4-fold larger. This is because the sign of the CD generated by the chiral material is opposite that generated from the chiral geometry at $\lambda = 740$ nm. These counteracting effects prevent the CD enhancement that one might expect from chiral patterning of chiral media. This becomes apparent when the geometry of the chiral arrangement is reversed, as shown in Fig. 7(c). When the enantiomeric structure is considered, the CD of the chiral arrangement at $\lambda = 740$ nm surpasses that of the disk array comprised of chiral material by 170%. This demonstrates how geometric and material chirality can sometimes compete, leading to nonobvious design choices that heavily depend on the wavelength of interest.

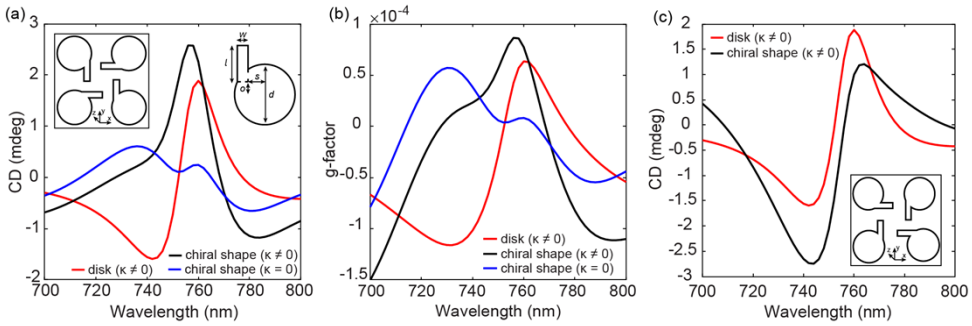

Fig. 7. (a) CD and (b) g-factor of the intrinsically chiral disk array (red line) compared to the C4 symmetric chiral shape array when $\kappa = -5 \times 10^{-6}i$ (black line) and when $\kappa = 0$ (blue line). Insets in (a) show pictorial representations of the C4 symmetric chiral unit cell. Each chiral shape has $d = 464$ nm, $l = 150$ nm, $w = 50$ nm, $o = 100$ nm, and $s = 159$ nm. (c) CD of the intrinsically chiral disk array (red line) compared to the enantiomeric chiral arrangement when $\kappa = -5 \times 10^{-6}i$ (black line). Inset shows the enantiomeric chiral arrangement.

4. Discussion and conclusions

Materials that selectively interact with circularly polarized light have wide-ranging applications from 3-D displays to optical communications. In this work, we modeled arrays of nanostructures consisting of chiral media to elucidate the design principles governing chiroptical activity. Future work could investigate these factors in 3-D chiral structures, such as those described in Gorkunov et al [48]. In this work, we were inspired by chiral patterning of light-emitting nanocrystals comprising the meta-atoms and motivated by applications like circularly polarized light sources, so we considered the optical chirality inside the nanostructures as opposed to only around the structures. By investigating percent of light transmitted, the optical chirality enhancement, and the electric and magnetic fields inside the nanostructures, we uncovered design factors that specifically influence the circular dichroism, g-factor, and relative transmission of LCP versus RCP light in chiral metasurfaces. We showed that disk arrays supporting overlapping electric and magnetic dipolar Mie-like resonances show significant CD enhancement compared to a uniform chiral film. We considered metasurfaces with real, imaginary, and complex Pasteur parameters

Optics EXPRESS

with varying magnitude and sign. When Mie-like disk arrays have a purely imaginary Pasteur parameter ($-0.0005i \leq \kappa \leq -0.05i$) the CD enhancement is 6-fold, and if the arrays have a purely real and physically relevant Pasteur parameter ($\kappa = 0.01$), the ΔT enhancement is over 750-fold. For Mie-like arrays with purely real Pasteur parameters, increasing the Pasteur parameter of the medium causes spectral shifts in the ED and MD resonances, diminishing the average optical chirality. By contrast, Mie-like arrays with purely imaginary Pasteur parameters do not exhibit spectral shifting of the ED and MD resonances and instead exhibit changes in the intensity of the electric and magnetic fields inside the meta-atoms depending on the magnitude of κ. Therefore, the average optical chirality increases with $|\kappa|$ when the Pasteur parameter is purely imaginary. Matching the Mie-like resonance to a chiral material's Lorentzian transition resulted in a hybrid light-matter resonance that led to a nearly 22-fold enhancement in CD compared to a chiral film. Further, constructing a geometrically chiral meta-atom out of chiral media led to over 9-fold enhancements in both CD and g-factor relative to an identical metasurface made from achiral material. These results expose several different design approaches for tailoring a chiral response from metasurfaces constructed from chiral media. Each of these design choices: nanopatterning, employing overlapping ED and MD resonances, increasing or decreasing the chirality of the medium, choosing a dispersive or non-dispersive medium, and selecting a chiral geometry, have different effects on the shape and magnitude of the CD and g-factor. This study provides a framework for understanding how these individual factors shape the chiroptical response, so that they may be employed in other chiral metastructures to satisfy specific design needs.

Funding. National Science Foundation (2102835).

Acknowledgement. The authors acknowledge the Minnesota Supercomputing Institute (MSI) at the University of Minnesota for providing resources that contributed to the research results within this paper.

Disclosures. Authors declare no conflicts of interest.

Data Availability. Data underlying the results presented in this paper are available in Ref. [49].

References

1. J. Cheng, J. Hao, H. Liu, *et al.*, "Optically Active CdSe-Dot/CdS-Rod Nanocrystals with Induced Chirality and Circularly Polarized Luminescence," ACS Nano **12**(6), 5341–5350 (2018).
2. Z. Wang, Y. Wang, G. Adamo, *et al.*, "Induced Optical Chirality and Circularly Polarized Emission from Achiral CdSe/ZnS Quantum Dots via Resonantly Coupling with Plasmonic Chiral Metasurfaces," Laser Photon. Rev. **13**(3), 800276 (2019).
3. J. Ma, C. Fang, C. Chen, *et al.*, "Chiral 2D Perovskites with a High Degree of Circularly Polarized Photoluminescence," ACS Nano **13**(3), 3659–3665 (2019).
4. C. Chen, L. Gao, W. Gao, *et al.*, "Circularly polarized light detection using chiral hybrid perovskite," Nat. Commun. **10**(1), 1927 (2019).
5. W. Chen, S. Zhang, M. Zhou, *et al.*, "Two-Photon Absorption-Based Upconverted Circularly Polarized Luminescence Generated in Chiral Perovskite Nanocrystals," J. Phys. Chem. Lett. **10**(12), 3290–3295 (2019).
6. C. Carrillo-Carrión, S. Cárdenas, B. M. Simonet, *et al.*, "Selective Quantification of Carnitine Enantiomers Using Chiral Cysteine-Capped CdSe(ZnS) Quantum Dots," Anal. Chem. **81**(12), 4730–4733 (2009).
7. C. Han and H. Li, "Chiral Recognition of Amino Acids Based on Cyclodextrin-Capped Quantum Dots," Small **4**(9), 1344–1350 (2008).
8. F. Gao, S. Ma, X. Xiao, *et al.*, "Sensing tyrosine enantiomers by using chiral CdSe/CdS quantum dots capped with N-acetyl-l-cysteine," Talanta **163**, 102–110 (2017).
9. F. Ghasemi, M. R. Hormozi-Nezhad, and M. Mahmoudi, "Time-Resolved Visual Chiral Discrimination of Cysteine Using Unmodified CdTe Quantum Dots," Sci. Rep. **7**(1), 890 (2017).
10. T. Delgado-Pérez, L. M. Bouchet, M. de la Guardia, *et al.*, "Sensing Chiral Drugs by Using CdSe/ZnS Nanoparticles Capped with N -Acetyl-L-Cysteine Methyl Ester," Chem. - Eur. J. **19**(33), 11068–11076 (2013).
11. H. Lu, J. Wang, C. Xiao, *et al.*, "Spin-dependent charge transport through 2D chiral hybrid lead-iodide perovskites," Sci. Adv. **5**(12), eaay0571 (2019).
12. B. P. Bloom, V. Kiran, V. Varade, *et al.*, "Spin Selective Charge Transport through Cysteine Capped CdSe Quantum Dots," Nano Lett. **16**(7), 4583–4589 (2016).
13. M. L. Solomon, J. Hu, M. Lawrence, *et al.*, "Enantiospecific Optical Enhancement of Chiral Sensing and Separation with Dielectric Metasurfaces," ACS Photonics **6**(1), 43–49 (2019).
14. A. García-Etxarri and J. A. Dionne, "Surface-enhanced circular dichroism spectroscopy mediated by nonchiral nanoantennas," Phys. Rev. B **87**(23), 235409 (2013).

Optics EXPRESS

15. M. Schäferling, D. Dregely, M. Hentschel, *et al.*, "Tailoring Enhanced Optical Chirality: Design Principles for Chiral Plasmonic Nanostructures," Phys. Rev. X **2**(3), 031010 (2012).
16. V. Bochenkov and T. Shabatina, "Chiral Plasmonic Biosensors," Biosensors **8**(4), 120 (2018).
17. S. Yoo and Q.-H. Park, "Metamaterials and chiral sensing: a review of fundamentals and applications," Nanophotonics **8**(2), 249–261 (2019).
18. M. L. Solomon, A. A. E. Saleh, L. V. Poulikakos, *et al.*, "Nanophotonic Platforms for Chiral Sensing and Separation," Acc. Chem. Res. **53**(3), 588–598 (2020).
19. J. Mun and J. Rho, "Surface-enhanced circular dichroism by multipolar radiative coupling," Opt. Lett. **43**(12), 2856 (2018).
20. A. S. Berestennikov, P. M. Voroshilov, S. V. Makarov, *et al.*, "Active meta-optics and nanophotonics with halide perovskites," Appl. Phys. Rev. **6**(3), 1–20 (2019).
21. J. Hu, M. Lawrence, and J. A. Dionne, "High Quality Factor Dielectric Metasurfaces for Ultraviolet Circular Dichroism Spectroscopy," ACS Photonics **7**(1), 36–42 (2020).
22. M. Puri and V. E. Ferry, "Circular Dichroism of CdSe Nanocrystals Bound by Chiral Carboxylic Acids," ACS Nano **11**(12), 12240–12246 (2017).
23. F. Purcell-Milton, A. K. Visheratina, V. A. Kuznetsova, *et al.*, "Impact of Shell Thickness on Photoluminescence and Optical Activity in Chiral CdSe/CdS Core/Shell Quantum Dots," ACS Nano **11**(9), 9207–9214 (2017).
24. A. Ben-Moshe, A. Teitelboim, D. Oron, *et al.*, "Probing the Interaction of Quantum Dots with Chiral Capping Molecules Using Circular Dichroism Spectroscopy," Nano Lett. **16**(12), 7467–7473 (2016).
25. F. P. Milton, J. Govan, M. V. Mukhina, *et al.*, "The chiral nano-world: chiroptically active quantum nanostructures," Nanoscale Horiz. **1**(1), 14–26 (2016).
26. U. Tohgha, K. K. Deol, A. G. Porter, *et al.*, "Ligand Induced Circular Dichroism and Circularly Polarized Luminescence in CdSe Quantum Dots," ACS Nano **7**(12), 11094–11102 (2013).
27. X. Gao, B. Han, X. Yang, *et al.*, "Perspective of Chiral Colloidal Semiconductor Nanocrystals: Opportunity and Challenge," J. Am. Chem. Soc. **141**(35), 13700–13707 (2019).
28. G. Long, C. Jiang, R. Sabatini, *et al.*, "Spin control in reduced-dimensional chiral perovskites," Nat. Photonics **12**(9), 528–533 (2018).
29. G. Long, Y. Zhou, M. Zhang, *et al.*, "Theoretical Prediction of Chiral 3D Hybrid Organic–Inorganic Perovskites," Adv. Mater. **31**(17), 1807628 (2019).
30. G. Long, R. Sabatini, M. I. Saidaminov, *et al.*, "Chiral-perovskite optoelectronics," Nat. Rev. Mater. **5**(6), 423–439 (2020).
31. T. H. Moon, S.-J. Oh, and K. M. Ok, "$[((R)\text{-}C_8H_{12}N)_4][Bi_2Br_{10}]$ and $((S)\text{-}C_8H_{12}N)_4][Bi_2Br_{10}]$: Chiral Hybrid Bismuth Bromides Templated by Chiral Organic Cations," ACS Omega **3**(12), 17895–17903 (2018).
32. O. Erdem, S. Foroutan, N. Gheshlaghi, *et al.*, "Thickness-Tunable Self-Assembled Colloidal Nanoplatelet Films Enable Ultrathin Optical Gain Media," Nano Lett. **20**(9), 6459–6465 (2020).
33. D. B. Dement, M. K. Quan, and V. E. Ferry, "Nanoscale Patterning of Colloidal Nanocrystal Films for Nanophotonic Applications Using Direct Write Electron Beam Lithography," ACS Appl. Mater. Interfaces **11**(16), 14970–14979 (2019).
34. A. Lakhtakia, V. K. Varadan, and V. V. Varadan, "Dilute random distribution of small chiral spheres," Appl. Opt. **29**(25), 3627 (1990).
35. D. L. Jaggard, A. R. Mickelson, and C. H. Papas, "On electromagnetic waves in chiral media," Appl. Phys. **18**(2), 211–216 (1979).
36. A. H. Sihvola and I. V. Lindell, "BI-isotropic constitutive relations," Microw. Opt. Technol. Lett. **4**(8), 295–297 (1991).
37. M. L. Nesterov, X. Yin, M. Schäferling, *et al.*, "The Role of Plasmon-Generated Near Fields for Enhanced Circular Dichroism Spectroscopy," ACS Photonics **3**(4), 578–583 (2016).
38. I. Staude, A. E. Miroshnichenko, M. Decker, *et al.*, "Tailoring Directional Scattering through Magnetic and Electric Resonances in Subwavelength Silicon Nanodisks," ACS Nano **7**(9), 7824–7832 (2013).
39. S. Yoo and Q.-H. Park, "Enhancement of Chiroptical Signals by Circular Differential Mie Scattering of Nanoparticles," Sci. Rep. **5**(1), 14463 (2015).
40. E. Hendry, R. V. Mikhaylovskiy, L. D. Barron, *et al.*, "Chiral Electromagnetic Fields Generated by Arrays of Nanoslits," Nano Lett. **12**(7), 3640–3644 (2012).
41. A. Ghosh and P. Fischer, "Chiral Molecules Split Light: Reflection and Refraction in a Chiral Liquid," Phys. Rev. Lett. **97**(17), 173002 (2006).
42. M. Schäferling, N. Engheta, H. Giessen, *et al.*, "Reducing the Complexity: Enantioselective Chiral Near-Fields by Diagonal Slit and Mirror Configuration," ACS Photonics **3**(6), 1076–1084 (2016).
43. S. Lee, S. Yoo, and Q.-H. Park, "Microscopic Origin of Surface-Enhanced Circular Dichroism," ACS Photonics **4**(8), 2047–2052 (2017).
44. K. Yao and Y. Liu, "Enhancing circular dichroism by chiral hotspots in silicon nanocube dimers," Nanoscale **10**(18), 8779–8786 (2018).
45. P. E. Stamatopoulou, S. Droulias, G. P. Acuna, *et al.*, "Reconfigurable chirality with achiral excitonic materials in the strong-coupling regime," Nanoscale **14**(47), 17581–17588 (2022).

Optics EXPRESS

46. J. Lasa-Alonso, D. R. Abujetas, A. Nodar, *et al.*, "Surface-Enhanced Circular Dichroism Spectroscopy on Periodic Dual Nanostructures," ACS Photonics **7**(11), 2978–2986 (2020).
47. M. Decker, R. Zhao, C. M. Soukoulis, *et al.*, "Twisted split-ring-resonator photonic metamaterial with huge optical activity," Opt. Lett. **35**(10), 1593 (2010).
48. M. V. Gorkunov, A. A. Antonov, and Y. S. Kivshar, "Metasurfaces with Maximum Chirality Empowered by Bound States in the Continuum," Phys. Rev. Lett. **125**(9), 093903 (2020).
49. M. Ramamurthy, B. M. Cote, and V. E. Ferry, "Data for Chiral Optical Properties of Metasurfaces Comprised of Chiral Media: Effects of Geometric and Material Chirality," Data Repository for the University of Minnesota (2024), https://doi.org/10.13020/8FZW-EJ78.